Design Considerations for 1.06-μm InGaAsP–InP Geiger-Mode Avalanche Photodiodes

Joseph P. Donnelly, *Life Fellow, IEEE*, Erik K. Duerr, K. Alex McIntosh, Eric A. Dauler, Douglas C. Oakley, Steven H. Groves, Christopher J. Vineis, Leonard J. Mahoney, Karen M. Molvar, Pablo I. Hopman, Katharine Estelle Jensen, Gary M. Smith, *Member, IEEE*, Simon Verghese, *Member, IEEE*, and David C. Shaver, *Senior Member, IEEE*

***Abstract*—For Geiger-mode avalanche photodiodes, the two most important performance metrics for most applications are dark count rate (DCR) and photon detection efficiency (PDE). In 1.06-μm separate-absorber-avalanche (multiplier) InP-based devices, the primary sources of dark counts are tunneling through defect levels in the InP avalanche region and thermal generation in the InGaAsP absorber region. PDE is the probability that a photon will be absorbed (quantum efficiency) times the probability that the electron–hole pair generated will actually cause an avalanche. A device model based on experimental data that can simultaneously predict DCR and PDE as a function of overbias and temperature is presented. This model has been found useful in predicting changes in performance as various device parameters, such as avalanche layer thickness, are modified. This has led to designs that are capable simultaneously of low DCR and high PDE.**

***Index Terms*—Avalanche photodiodes, Geiger-mode avalanche photodiodes, photodiodes, semiconductor device modeling, single-photon detection.**

I. Introduction

GEIGER-MODE avalanche photodiode arrays are receiving increased interest for a number of photon counting applications, including astronomy, three-dimensional laser radar (LADAR) [1]–[4] and photon-counting optical communication [5], [6]. In Geiger-mode operation, the avalanche photodiode is biased above breakdown. This is a metastable state since the generation of an electron–hole pair, either thermally or through absorption of a photon, can cause the diode to break down. Breakdown produces a rapid rise in current, which ultimately becomes limited by series resistance and internal space-charge effects. Since the Geiger-mode APD is initially biased a few volts above breakdown, the breakdown event produces a large signal swing, which can directly drive CMOS digital logic [1], [2]. This is an important attribute of these devices and has allowed the development of Geiger-mode arrays bonded directly to readout integrated circuits (ROICs). The ability to make arrays and read them out at high data rates is important for both LADAR [1]–[4] and optical-communications applications [5], [6]. The use of an all-digital readout reduces power, and makes the technology more easily scalable to large array sizes than competing technologies, which employ linear-mode APDs or photomultiplier tubes.

Geiger-mode devices can be characterized by two major parameters: photon detection efficiency (PDE) and dark count rate (DCR). Since the digital readout of Geiger-mode devices is essentially noiseless, noise in Geiger-mode APDs is associated with dark counts (false ones), due to thermally generated carriers or tunneling current in the APD or optical background photons, and false zeros, which arise from less than perfect detection of incident signal photons. This concept of noise differs from the "excess noise" [7] of linear-mode APDs, which depends on the ionization coefficient ratio [8]. The ratio of ionization coefficients does play a role in the Geiger mode, in that it affects the probability of avalanche and, therefore, the probability of detection, as a function of overbias. For improving Geiger-mode APD performance, reducing the DCR without degrading PDE is extremely important and can be affected by device design, material quality and operating parameters. As will be shown, PDE can be increased to quite high values by increasing overbias while still maintaining acceptable DCRs.

In this paper, a self-consistent model based on fits to experimental data on appropriate test structures is developed and used to predict performance of 1.06-μm InGaAsP–InP Geiger-mode APDs. The major sources of dark current responsible for dark count rates in devices designed for 1.06-μm operation will be discussed and ways of minimizing them presented. Probability of detection will then be discussed, along with optimization of device parameters for low DCR and high PDE. For many applications, other parameters, such as turn-on jitter and reset time, must also be considered. Reset time is especially important for laser communications. It is the time the APD bias voltage must be held below breakdown after it has fired to avoid afterpulsing [9]–[12]. These parameters with possible tradeoffs required to meet overall requirements for a particular application will be treated in other publications.

II. Device Structure

The APD structure is schematically shown in Fig. 1. It is essentially an inverted mesa structure with separate absorber, grade, field-stop or charge layer, and avalanche (multiplier) region. A structure of this type is often referred to as a SAM or SAGCM structure. Since tunneling is an issue in these devices, a field-stop layer is employed to control and minimize the peak fields in various parts of the APD. With an inverted mesa, the

Manuscript received February 10, 2006; revised April 3, 2006. This work was supported by the National Aeronautics and Space Administration under Air Force Contract FA8721-05-C-0002. Opinions, interpretations, conclusions, and recommendations are those of the author and are not necessarily endorsed by the U.S. Air Force.

The authors are with the Lincoln Laboratory, Massachusetts Institute of Technology, Lexington, MA 02420 USA (e-mail: Donnelly@ll.mit.edu).

Digital Object Identifier 10.1109/JQE.2006.877300

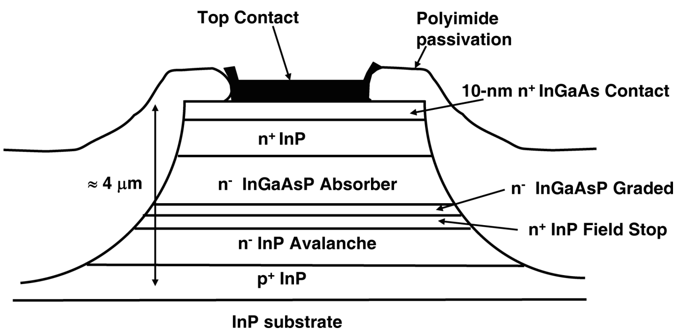

Fig. 1. Schematic of 1.06-μm wavelength InGaAsP–InP Geiger-mode avalanche photodiode.

slope of the sidewalls in the high-field regions is used to suppress edge breakdown.

The APD structures were grown by organo-metallic vapor phase epitaxy on (100) InP substrates. As discussed below, we have used p^+-, n^+-, and n^--InP substrates. A two step p^+-InP layer is grown first to serve as the p-side of the junction. The lower part is 1.5-μm thick and has a doping of 2×10^{18} cm^{-3}, while the upper part is 0.5-μm thick and has a doping of 1×10^{18} cm^{-3}. The nominally undoped InP avalanche region of thickness W_A(0.8–2.0 μm) is grown next and has a n-type concentration $\leq 10^{15}$ cm^{-3}. This is followed by a heavily doped n^+-InP ($N_{\rm FS} = 3.5$–7.0×10^{17} cm^{-3}) field stop layer of thickness $W_{\rm FS}$. The $N_{\rm FS}W_{\rm FS}$ product is chosen so that: 1) the absorber layer is fully depleted before breakdown at the lowest temperature of operation and 2) the maximum field in the absorber is $\leq 1.0 \times 10^5$ V/cm at the maximum overbias at the highest temperature of operation. The first criterion assures that photo-carriers generated anywhere in the absorber are swept quickly to the avalanche region reducing jitter. In Geiger-mode operation, it is not absolutely essential to have the absorber fully depleted at breakdown, but only at the operating overbias. To obtain consistent comparisons of DCR and PDE between different structures as functions of temperature and overbias, we have restricted this paper to devices in which the absorber is fully depleted at breakdown. The second criterion minimizes any field-enhanced dark current in the absorber. A 50-nm-thick compositionally graded InGaAsP layer is then grown to facilitate transfer of photo-generated holes from the absorber to the avalanche region. The nominally undoped InGaAsP absorber ($n \leq 10^{15}$ cm^{-3}) of thickness $W_{\rm Abs}$ (nominally 1.5 μm) is then grown. This is followed by an n^+-InP layer and a 10-nm-thick n^+-InGaAs contact layer.

Following mesa etching, polyimide passivation is applied and ohmic contacts made to the top of the mesa. For top illuminated devices, an annular contact is used, while for back-illuminated devices a circular-disk contact is used. Anode contacts are either made to the back of the substrate or on the top to the etched p^+-InP layer. For back-illumination, wafers are thinned to 150 μm and antireflection coatings applied. In this case, circular openings in any back metal are left under each APD.

We started by investigating top-illuminated devices and employed p^+-InP substrates with back metallization [13], [14]. Back-illumination allows for smaller diodes and bump bonding of arrays directly to ROIC readouts [1]–[4], [6]. Because the p^+-InP substrates were very lossy ($\approx 30\,\mathrm{cm}^{-1}$), we switched to n^+-InP substrates, which had significantly lower loss. N^+-InP substrates were originally chosen over even lower loss n^-- or iron-doped substrates because: 1) highly doped substrates have orders of magnitude lower etch pit densities and there are anecdotal data that indicate leaky or shorted diodes are often associated with dislocations and 2) some ROICs that were being used required back anode contacts and the n^+-substrates allowed for a tunnel or backward junction between the p^+-buffers and the substrate and also reduced series resistance and electrical crosstalk between diodes in an array. For some arrays, anode contacts are now being made on and brought out from the top of the wafer. Since the use of n^--substrates for back-illuminated devices can reduce substrate losses to insignificant values, thereby increasing PDE, we have begun investigating the use of n^- as well as n^+-substrates. To date, the yield on small arrays seems acceptable. Additional information on the focal-plane array concept with the APD array directly bump bonded to CMOS ROICs, including the operation of the pixel elements, can be found in [1], [4], and [6].

III. Ionization Coefficients

Both breakdown voltage and probability of avalanche above breakdown depend on the ionization coefficients in the InP avalanche region. There are numerous reports of InP ionization coefficients in the literature [15]–[20], all of which show a higher ionization coefficient for holes than electrons. Most of these were measured on InP p-n junctions designed to allow both pure hole and electron injection into the high field region. The ionization coefficients were then derived from the measured photocurrent gain and the known electric-field profile versus voltage (below breakdown) and the breakdown voltage in the structure. Unfortunately, there is not a great deal of agreement between the reported results, besides which ioization coefficient is higher, indicating the difficulty of determining these coefficients. In addition, the measurements were generally carried out only at room temperature. Because of these inconsistencies and because none of the published ionization coefficient pairs were consistent with the breakdown voltages measured on their devices, Zappa *et al.* [21] proposed a quasi-physical model [22], [23], which explicitly contained a temperature dependence for the ionization coefficients.

We had similar difficulties fitting our room-temperature data to any of the published ionization coefficients. In addition to obtaining a best fit to breakdown voltage, we also attempted to fit the DCR and PDE as a function of overbias as discussed below. The ionization coefficients model we selected uses another quasi-physical model [24], with several adjustable parameters. The selected ionization coefficients used to obtain a best fit to data were for holes

$$\beta(F,T) = \frac{F}{E_{th\_h}} \exp\left(-\frac{E_{th\_h}}{(F\lambda_h)^2/(3E_{P\_h}) + F\lambda_h + kT}\right) \tag{3.1}$$

where F is the field in volts per centimeter, k is Boltzmann's constant in electron volts, T is the temperature in degrees Kelvin, $E_{th\_h} = 1.45$ eV, $\lambda_h = 5.38 \times 10^{-7}$ cm $*$

$\tanh(E_{p0\_h}/2kT)$, $E_{p\_h} = E_{p0\_h}\tanh(E_{p0\_h}/2kT)$, and $E_{p0\_h} = 36$ meV, and for electrons

$$\alpha(F,T) = \frac{F}{E_{th\_e}}\exp\left(-\frac{E_{th\_e}}{(F\lambda_e)^2/(3E_{P\_e}) + F\lambda_e + kT}\right) \tag{3.2}$$

where $E_{th\_e} = 1.60$ eV, $\lambda_e = 4.73 \times 10^{-7}$ cm $*$ $\tanh(E_{p0\_e}/2kT)$, $E_{p\_e} = E_{p0\_e}\tanh(E_{p0\_e}/2kT)$, and $E_{p0\_e} = 46$ meV.

In our calculations, we assume that the coefficients are dependent only on field (i.e., we ignore acceleration or dead space effects [25]–[28]), since we will be dealing with very wide avalanche regions in which the field is fairly constant). These ionization coefficients have an explicit temperature dependence and are easily adjustable up and down by making small changes in the mean free path parameters λ_h and λ_e. They in fact can be made to fit fairly accurately most of the published ionization coefficients.

To compare the predictions of the different ionization coefficient pairs, for the structure illustrated in Fig. 1, we computed the breakdown voltage and the probability that a hole injected into the high field region from the absorber causes a breakdown event when the diode is biased above breakdown. This probability of avalanche (PA) is discussed more fully in Section IV. Results of these calculations using the above ionization coefficient models and several ionization coefficient pairs published in the literature are plotted in Fig. 2. The nominal structure used in the calculations had a 1.0-μm-thick avalanche region, a 50-nm-thick graded layer, and a 1.5-μm-thick absorber region. The field stop had a carrier concentration of 7×10^{17} cm^{-3} and a thickness of 38 nm. For these calculations, the field at the beginning of the field-stop region was recursively iterated and the field at each point calculated until the breakdown ionization integral

$$\mathrm{BI} = \int_0^W \beta(x)\exp\left(\int_0^x (\beta(x') - \alpha(x'))dx'\right)dx \tag{3.3}$$

was equal to one [7]. Here $x = 0$ corresponds to the beginning of the field stop layer and $W = W_{\mathrm{FS}} + W_A + W_p$ is the edge of the depletion layer in the p$^+$-InP.

Small increments in the field at the beginning of field-stop region were then made to simulate overbias and, for each step, the field at each point calculated. The field at each point was needed not only to calculate the ionization integral, but to calculate PA, tunneling currents, etc. For each step, the total voltage across the structure was easily obtained from the field at the beginning of the field-stop region. The built-in voltage was subtracted from the total voltage to obtain the applied or external voltage.

The points where the probability-of-avalanche curves go to zero in Fig. 2 indicate the calculated breakdown voltages for the different ionization coefficient sets. Note that different reported ionization coefficients predict both higher and lower breakdown voltages than experimentally observed (as given by curve labeled "This Work") and fit using the ionization coefficient models described above. Breakdown voltage was not the only criterion used in determining the ionization coefficient models selected. Both DCR and PDE versus overbias were considered since these depend on PA versus overbias and as can be seen

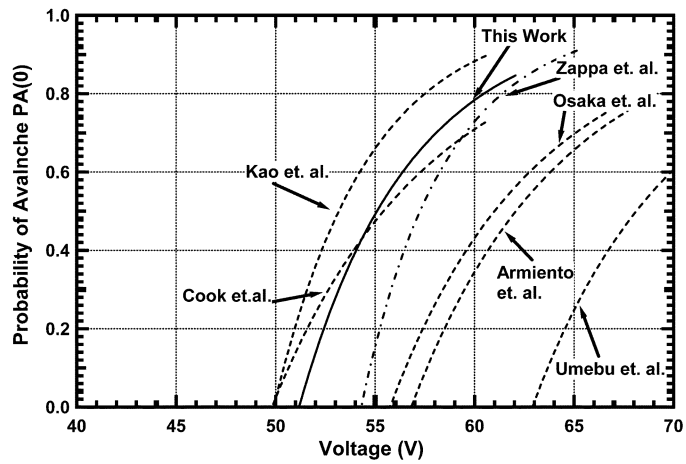

Fig. 2. Probability of avalanche for a hole injected into the avalanche region from the absorber PA(0) versus voltage for several different ionization coefficient pairs [13]–[19]. The APD has a 1.0-μm-thick avalanche region and a 1.5-μm-thick absorber.

in the figure, PA depends on the ionization coefficients. Since $\beta > \alpha$ in InP, hole injection is advantageous for obtaining a high PA. For holes injected from the absorber into the avalanche region, a larger β/α ratio results in a more rapid increase of PA with overbias and, thus, a smaller overbias is required for a desired PA. Some fine tuning of the ionization coefficient models is expected in the future as more data is collected, but the coefficient models selected fit our data and can be used to predict performance in new designs and at reduced temperature.

IV. Probability of Avalanche

The probability of avalanche is a key concept in calculating DCR and PDE. Since each ionization event is probabilistic, the likelihood of an actual breakdown occurring due to a single electron–hole pair will also be probabilistic. PA will increase with overbias, the rate of increase depending on the ratio of the ionization coefficients. PA will also depend on the position where an electron–hole pair is generated. Following McIntyre's [29] derivation of PA(x) and assuming field-dependent ionization coefficients (i.e., ignoring nonlocal effects such as acceleration of carriers in these devices with wide avalanche regions), PA for hole injection into the avalanche region from the absorber, PA(0), can be found by solving the following:

$$\mathrm{PA}(0) = 1 - \exp\left(-\int_0^W \beta(x')\mathrm{PA}(x')dx'\right) \tag{4.1}$$

where $x = 0$ corresponds to the beginning of the FS region and $x = W = W_{\mathrm{FS}} + W_A + W_P$ to the edge of the depletion region in the p$^+$- region (W_P being the depletion depth in the p$^+$-InP)

$$\mathrm{PA}(x) = \frac{\mathrm{PA}(0)f(x)}{\mathrm{PA}(0)f(x) + 1 - \mathrm{PA}(0)} \tag{4.2}$$

is the probability of avalanche for an electron–hole created at x, where

$$f(x) = \exp\left(\int_0^x (\alpha(x') - \beta(x'))dx'\right)$$

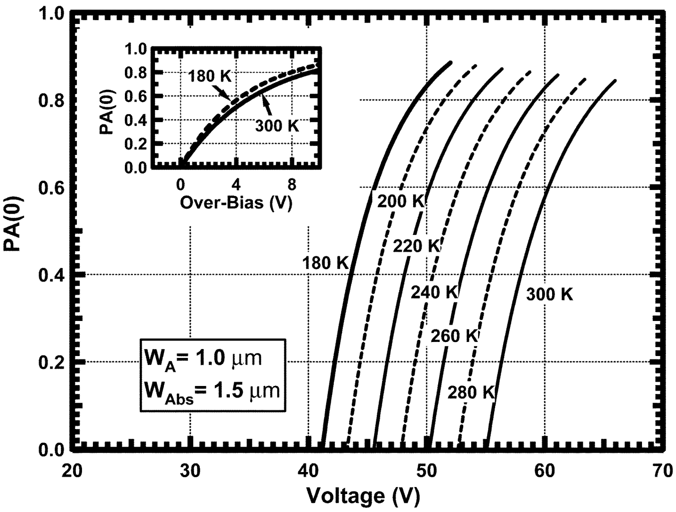

Fig. 3. PA(0) versus voltage for several different temperatures. The APD has a 1.0-μm-thick avalanche region and a 1.5-μm-thick absorber. The field stop doping-thickness product was adjusted so that the absorber would be fully depleted before breakdown at 180 K. Inset shows PA(0) versus overbias.

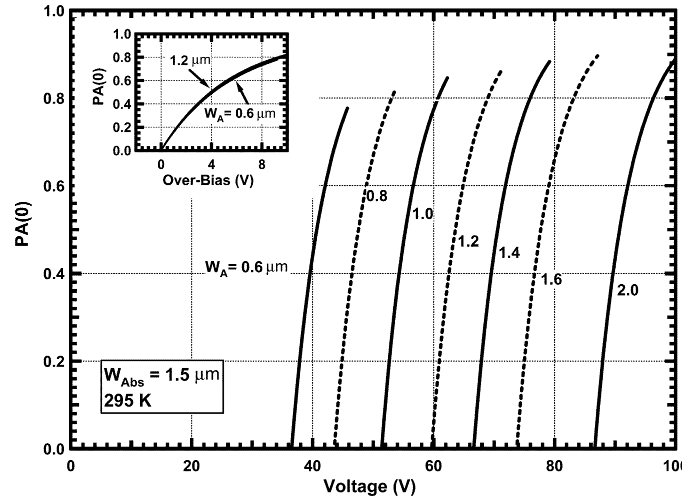

Fig. 4. PA(0) versus voltage for several different avalanche thicknesses at 295 K. All devices had a 1.5-μm-thick absorber. The field stop doping-thickness product was adjusted in each case so that the absorber would be fully depleted before breakdown. Inset shows PA(0) versus overbias.

and $\beta(x)$ is the hole-ionization and $\alpha(x)$ the electron-ionization coefficient at x.

PA(0) is plotted as a function of voltage and temperature in Fig. 3 for a device with a 1.0-μm-thick avalanche region, an $n = 7 \times 10^{17}\text{cm}^{-3}$, 36-nm FS, and a 1.5-$\mu$m-thick absorber. The FS thickness was reduced for these plots from that used in Fig. 2 to insure punch-through before breakdown at 180 K. This results in slightly higher breakdown voltages. PA(0) versus overbias is shown in the inset. As the temperature is reduced, the ionization coefficients increase due to reduced carrier scattering. This results in a reduction in breakdown voltage ($\approx 0.1\ \text{V}/1\ \text{K}$). At the lower breakdown field strengths, the β/α ratio increases slightly resulting in a faster increase in PA with overbias. PA(0) versus voltage at 295 K for several avalanche thicknesses is shown in Fig. 4. As the avalanche thickness increases, the breakdown voltage increases. PA(0) versus overbias, however, does not change much with increasing avalanche thickness as indicated in the inset. For the ionization coefficients used, there is a shallow maximum around $W_A \approx 1.2\ \mu$m due to a tradeoff between higher β/α ratios at lower fields and smaller increases in field with overbias as the avalanche region thickness increases.

For electron–hole pairs generated in the avalanche region, PA(x) can be found from PA(0) using (4.2) and is plotted for several different overbiases in Fig. 5. This type of electron–hole pair can arise from thermal generation or tunneling in the avalanche region or from electroabsorption of photons in the high-field region. Note that PA is highest for hole injection and lowest for electron injection as expected. Electron–hole pairs generated in the avalanche region, therefore, generally have a lower probability of causing an avalanche than those generated in the absorbing layer.

V. Dark Count Rate

DCR is one of the most important parameters in a Geiger-mode APD. If the DCR can be kept low, appropriate overbiases can be used to obtain high PA. In many devices DCR, however, increases faster than PA with overbias, limiting the maximum

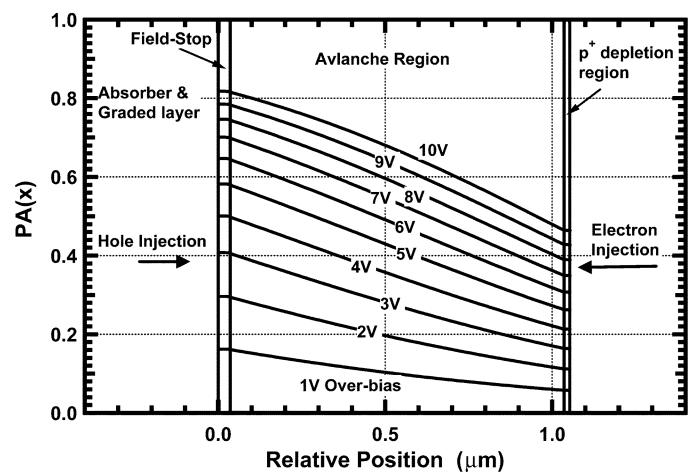

Fig. 5. Probability of avalanche as a function of position PA(x) for electron–hole pairs generated in the avalanche region at 295 K for several different overbiases. The APD has a 1.0-μm-thick avalanche region and a 1.5-μm-thick absorber.

overbias voltage that can be used. It is, therefore, extremely important to understand the sources of dark counts to appropriately design the APD for both low DCR and high PDE.

Sources of dark counts are tunneling and thermal-generation currents in the different sections of the device. Thermal-generation rates, even in these direct gap semiconductors, are dominated by defects and depend on the crystal quality of the material. The material quality can usually be associated with a lifetime, τ, and thermal generation written simply as n_i/τ, where n_i is the intrinsic carrier concentration of the material, which depends on both bandgap and temperature. Since generation is of any significance only around room temperature on devices with very wide avalanche regions, for simplicity, τ has been assumed a constant independent of temperature and field. In considering tunneling currents, both direct band-to-band tunneling [30], [31] as well as tunneling through defect [32] states in the bandgap as illustrated in Fig. 6 must be considered. We have found that in our devices, defect tunneling in the InP avalanche

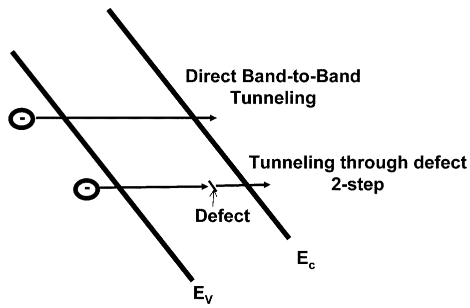

Fig. 6. Schematic illustration of direct band-to-band tunneling and tunneling through a defect.

region is much higher than direct band-to-band tunneling and must be modeled appropriately. Tunneling in the absorber (both direct and through defects or traps) must also be considered in the APD design. The total DCR per unit area in a typical APD structure can then be written as

$$\begin{aligned}\mathrm{DCR} = &\int_0^W \left(\left(\frac{n_{i\_InP}}{\tau_{InP}}\right) + \frac{J_{\mathrm{tun\_Av}}(x)}{q}\right) \mathrm{PA}(x)dx \\ &+ \mathrm{PA}(0)\int_0^{W_{Gd}} \left(\left(\frac{n_{i\_Gd}(x)}{\tau_{IGd}}\right) + \frac{J_{\mathrm{tun\_Gd}}(x)}{q}\right) dx \\ &+ \mathrm{PA}(0)\left(\left(\frac{n_{i\_Abs}}{\tau_{\mathrm{Abs}}}\right) W_{\mathrm{Abs}} \right.\\ &\left.\qquad + \int_0^{W_{\mathrm{Abs}}} \frac{J_{\mathrm{tun\_Abs}}(x)}{q} dx\right) \end{aligned} \tag{5.1}$$

where q is the electronic charge and $W = W_{\mathrm{FS}} + W_A + W_p$, Subscript Av in, for example, (5.1) denotes the entire avalanche region (including field-stop and depletion in p$^+$), Gd the graded region and Abs the absorber. Tunneling in the avalanche region (including the field-stop and depleted p$^+$ region) is given by

$$J_{\mathrm{tun\_Av}}(x) = J_{\mathrm{tun\_Av\_dir}}(x) + J_{\mathrm{tun\_Av\_def}}(x).$$

Tunneling in the absorber and graded regions also consist of direct and defect-assisted tunneling terms. Here the units of J are amperes per cubic centimeter, and J must be integrated over x to give current densities in units of amperes per square centimeter.

We have neglected any diffusion current, i.e., generation of carriers in the nondepleted sections of the device, which diffuse to the depletion layer, since these currents will be small. Generation and tunneling currents in the thin graded region are small, but are included in the calculations for completeness. Generation current in the InP will usually be small compared to both generation current in the absorber and tunneling in the avalanche region. To keep tunneling currents in the absorber negligible, the maximum field in the absorber at the highest overbias must be kept small by appropriately choosing the field-stop doping and thickness. Since the breakdown voltage and, therefore, the fields at any overbias are temperature dependent, some consideration of the temperature operating range must be taken into account in choosing an appropriate field-stop for a particular design. For devices with InGaAsP 1.06-μm absorbers, this maximum field in the absorber is rather high ($\approx 2 \times 10^5$ V/cm), and there is some latitude in the field-stop parameters and temperature over which the APD can be operated.

For tunneling current in the avalanche region, we have used the usual tunneling equation for direct band-to-band tunneling [30], [31] and a single trap level model for tunneling through a defect as illustrated in Fig. 6. For direct tunneling, we have

$$J_{\mathrm{tun\_Av\_dir}}(x) = A\,F(x)^2 \exp\left(\frac{-B\,E_g^{3/2}}{F(x)}\right) \tag{5.2}$$

where $F(x)$ is the electric field at x, E_g is the bandgap (which is a function of temperature), $A = q^3(2m_r/(qE_g))^{1/2}/(4\pi^3\hbar^2)$, and $B = \pi(m_r/2)^{1/2}/(2q\hbar)$, where $m_r = 2(m_c m_{lh})/(m_c + m_{lh})$ is the reduced effective mass, m_c being the conduction band effective mass and m_{lh} being the light hole effective mass and $\hbar = h/2\pi$, h being Planck's constant. This model assumes a parabolic barrier [30], [31] and neglects heavy hole tunneling. It also neglects transverse carrier momentum [30], [31], which reduces tunneling.

For tunneling through a defect, we must consider the filling of the defect. Setting the tunneling current from the valence band to the defect equal to the tunneling current from the defect to the conduction band, the average defect filling is determined leading to a tunneling current given by

$$\begin{aligned}&J_{\mathrm{tun\_Av\_def}}(x) \\ &\quad= \frac{AF(x)^2 N_T \exp\left(\frac{-\left(B_1 E_{B1}^{3/2} + B_2 E_{B2}^{3/2}\right)}{F(x)}\right)}{N_v \exp\left(\frac{-B_1 E_{B1}^{3/2}}{F(x)}\right) + N_c \exp\left(\frac{-B_2 E_{B2}^{3/2}}{F(x)}\right)}\end{aligned} \tag{5.3}$$

where $B_1 = \pi(m_{lh}/2)^{1/2}/(2q\hbar)$, $B_2 = \pi(m_c/2)^{1/2}/(2q\hbar)$, E_{B1} = barrier height of tunneling from valence band to trap and is equal to $aE_g (a < 1)$, E_{B2} = barrier height of tunneling from trap to the conduction band and is equal to $(1-a)E_g$. N_v and N_c are the light-hole valence and conduction band density of states and N_T represents the number of defects per unit volume and is used as a fitting parameter much like τ is used in determining the thermal generation currents. There are two parameters which determine the tunneling through defects, the position of the defect, a, and the number, N_T. This defect tunneling model ignores many issues, such as transverse momentum considerations, the exact shape of the barriers, etc., but as shown below, it can be used to obtain excellent fits to experimental data.

To obtain appropriate parameters for tunneling through defects in InP, we grew a number of different test APD structures with dummy InP absorber layers (instead of the usual InGaAsP absorber) and measured the DCR versus overbias. Parameters were then varied to obtain best fits to the data. In addition to the position of the defects in the bandgap and the number of defects, other ionization coefficient pairs were used to determine the best fits to DCR data. Although we included generation and direct tunneling in the fits, these structures were found to be dominated by tunneling through defects. Defect-assisted tunneling is 1 to 2 orders of magnitude greater than direct band-to-band tunneling in our current InP material. Best fits to the data were obtained with the position of the trap $0.75E_g$ above the valence band ($a = 0.75$). This is a position where there are known traps and

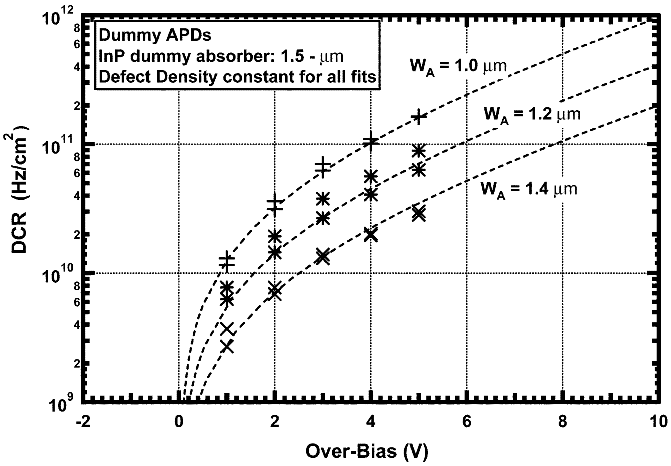

Fig. 7. Experimental and calculated DCRs versus overbias on APDs with several different avalanche thicknesses and 1.5-μm-thick dummy InP absorbers.

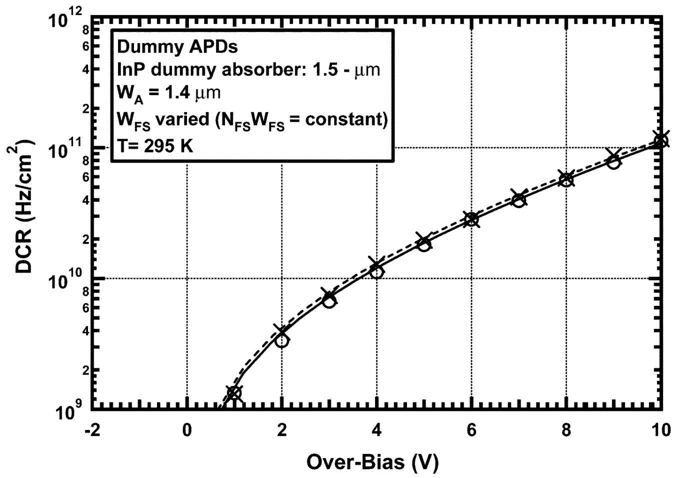

Fig. 8. Experimental and calculated DCRs versus overbias on more recent APDs with 1.4-μm-thick avalanche regions and 1.5-μm-thick dummy InP absorbers. The APDs had different thickness field stops, but the same carrier-concentration thickness product.

where the Fermi level tends to pin at InP surfaces and in material with high defect densities (caused by proton bombardment, etc.). The number of defects was fairly consistent from sample to sample and was typically around $N_T/N_C = (4–8) \times 10^{-4}$. The number is given in terms of N_C to stress that it should be considered more a fitting parameter than a precise measure of the actual trap density. Fig. 7 shows fits to the DCRs of three structures with different avalanche layer thicknesses: 1.0, 1.2, and 1.4 μm. All structures had 1.5-μm-wide dummy InP absorber layers. The field-stop thickness was adjusted downward with increasing avalanche thickness to keep the maximum field in the absorber region approximately constant. The DCR for each structure was calculated using the same fitting parameters for a and N_T (referred to as $N_{T\mathrm{nom}}$). In converting the measured DCRs to DCR per unit area, the active diameter of each device was assumed to be 5 μm less than the physical diameter to account for edge effects as discussed in Section VI. Fits to two more recent structures with 1.4-μm avalanche regions are shown in Fig. 8. These structures had thicker and lower doped (with the same concentration-thickness product) field-stop layers than the APD with a 1.4-μm avalanche region shown in Fig. 7. A slightly lower $N_T(\approx 0.6N_{T\mathrm{nom}})$ was used in fitting the data taken on these diodes indicating an improvement in material quality. In all cases N_T was always within a factor of 2 of the nominal value. The fits in Fig. 8 indicate that the DCR can be modeled quite accurately out to 10-V overbias.

With a good model for tunneling in the avalanche region, fits to DCRs in actual Geiger-mode APDs may now be carried out. A good model for defect tunneling in the absorber regions has not yet been obtained, but this is only of secondary consideration, since it is assumed that the APD will be designed with an appropriate field-stop layer so that the maximum field in the absorber is sufficiently low at the maximum overbias used to keep absorber tunneling current negligible. As a conservative approximation to make sure maximum field in the absorber is sufficiently low, we have modeled defect tunneling in InGaAsP as having ten times the number of defects as in the InP avalanche region. We also placed them slightly lower in the bandgap using a linear extrapolation with composition so that the defect level would be at midgap in latticed-matched InGaAs.

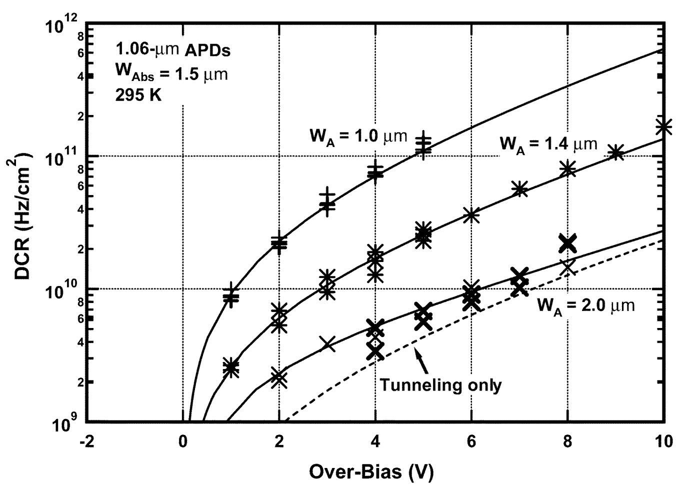

Fig. 9. Experimental and calculated DCRs versus overbias on 1.06-μm wavelength APDs with several different avalanche thicknesses and 1.5-μm-thick InGaAsP absorbers.

In 1.06-μm-wavelength APDs, tunneling in the InP avalanche region can be a main source of dark counts even at room temperature. Fits to the DCR per unit area of 1.06-μm APDs with 1.0-, 1.4-, and 2.0-μm avalanche regions are shown in Fig. 9. These devices had a 1.5-μm-thick absorber with a bandgap of $E_{g2} \approx 1.05$ eV$(\lambda_{g2} \approx 1.18\ \mu$m). All of the fits were carried out using a value for $N_T \approx 0.7N_{T\mathrm{nom}}$ for tunneling current in the avalanche region and a lifetime τ of 40 μs in the absorber. This lifetime is quite large indicating high quality material. The lower value of N_T used to fit these devices and the most recent InP dummy APDs indicate that the InP material quality is improving. Also shown is the DCR attributable only to tunneling in the avalanche region for the devices with 2.0-μm avalanche regions to give some idea of the portion of DCR due to generation current in the absorber.

Since the breakdown voltage decreases with decreasing temperature, the DCR even in devices dominated by tunneling in the avalanche region decreases significantly as the temperature

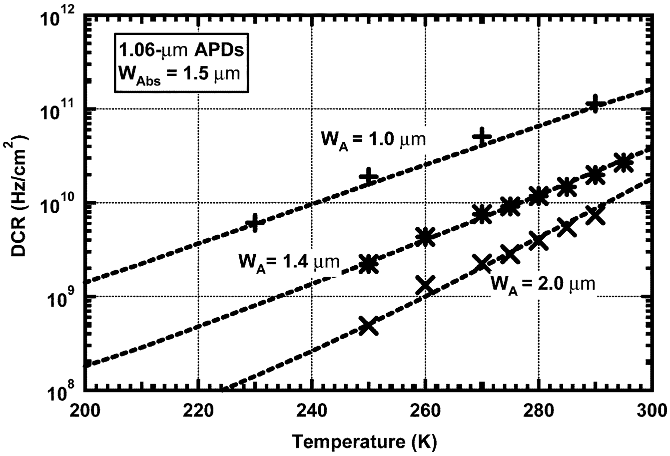

Fig. 10. Experimental and calculated DCRs versus temperature at 4-V overbias on 1.06-μm wavelength APDs with several different avalanche thicknesses and 1.5-μm-thick InGaAsP absorbers.

of operation is reduced. The DCR per unit area versus temperature of several devices with different avalanche layer thicknesses at 4-V overbias is shown in Fig. 10. These devices are from different runs than the devices shown in Fig. 9. In particular the device with the 1.0-μm-thick avalanche region comes from an older wafer and has a larger DCR than the comparable devices shown in Fig. 9 and an $N_T \approx 1.2 N_{T\text{nom}}$ was required for the fit versus temperature. The room temperature DCRs on the other devices are also slightly higher than the average DCR fit of Fig. 9 indicative of run-to-run and device-to-device variation. An $N_T \approx 0.9 N_{T\text{nom}}$ gave the best fit for these devices. Overall, the fit to the temperature dependence is quite good.

With the tunneling and lifetime fitting parameters established, DCRs can be calculated for various structures for different temperatures of operation. An $N_T = N_{T\text{nom}}$ and a lifetime of $\tau = 20\ \mu$s were used in these calculations and all calculations shown below to allow for slightly lower quality material and device-to-device variations. The calculated DCRs per unit area for 1.06-μm APDs with avalanche thicknesses of 1.0-, 1.4-, and 2.0-μm-thick avalanche regions at 240 and 280 K (temperatures easily reached by thermoelectric coolers) are shown in Fig. 11(a) and (b), respectively. The lower dark count rates at the lower temperature are due to a decreased breakdown voltage (lower field), which results in reduced tunneling in the avalanche region, as well as a reduction in n_{i_Abs} with decreasing temperature. For a diode with a 10-μm-diameter active region, DCRs of $\approx$ 10 kHz can be achieved at 280 K at 5-V overbias with a 1.4-μm avalanche region and at 10-V overbias with a 2.0-μm avalanche region. DCRs less than 1 kHz are possible at 240 K. Even lower DCRs are possible at lower temperatures. Although there are tradeoffs with PDE, as discussed in Section VI, devices with thicker avalanche regions are generally capable of higher overall performance but require slightly higher overbiases for the same PDE and a higher dc operating voltage. These factors can challenge the ROIC design and some compromises may be required.

VI. Probability of Detection

The probability of detection can be thought of as the probability of a photon being absorbed, creating an electron–hole pair, times the probability that this electron–hole pair will cause a sustained avalanche. If photons were only absorbed in the InGaAsP absorber region, this would be essentially the quantum efficiency (QE) of the diode (i.e., electron flow in the external circuit per incident number of photons if there was no gain) times the probability of avalanche for hole injection into the avalanche region PA(0). For 1.06-μm wavelength devices, however, electron–hole pair generation via electroabsorption [33]–[35] in the high field avalanche region must also be taken into account. Electron–hole pairs generated in the avalanche region via electroabsorption will lower the overall PDE of back-illuminated devices since the probability of avalanche PA$(x) \leq$ PA(0). In addition, reflections and any photons lost to free-carrier absorption before reaching the active region must also be taken into account. Although free carrier absorption takes place in all of the doped layers, it is generally only of significance in back-illuminated devices with heavily doped substrates. We will look at three cases: 1) front-illuminated devices where free carrier absorption is negligible and the photon passes through the absorber before reaching the avalanche region; 2) back-illuminated devices on lightly doped substrates where free carrier absorption is small and the photon passes through the avalanche region first; and 3) back-illuminated devices on highly doped substrates where free carrier absorption is substantial. Highly doped substrates are used because of their lower defect densities and for applications where it is necessary to make the common anode contact on the back of the device.

In general, a PDE of front-illuminated devices (for a single pass through the absorber) is given by (6.1), shown at the bottom of the page, where the first term in the bracket represents PDE due to absorption in the absorber, the second term to absorption in the graded layer and the third term to electroabsorption in the avalanche region. The contribution to PDE due to absorption in the graded layer is small. The start of the field stop region is at $x = 0$ and $W = W_A + W_{\text{FS}} + W_P$. The absorption coefficient in the absorber, α_{Abs}, is modeled as

$$\alpha_{\text{Abs}} = C * (h\nu - E_{g2})^{1/2}$$

where $C = 3.6 \times 10^4\ \text{cm}^{-1}\text{eV}^{-1/2}$ for the InGaAsP material used in the 1.06-μm devices. Since the absorber bandgap, E_{g2}, increases with decreasing temperature, α_{Abs} will decrease slightly with decreasing temperature. This is compensated by

$$\begin{aligned}\text{PDE} = (1-R)\Bigg\{&\text{PA}(0)(1-\exp(-\alpha_{\text{Abs}}W_{\text{Abs}})) + \exp(-\alpha_{\text{Abs}}W_{\text{Abs}})\text{PA}(0)\int_{-W_{Gd}}^{0}\alpha_{Gd}(x)\exp\left(-\int_{-W_{Gd}}^{x}\alpha_{Gd}(x')dx'\right)dx\\ &+\exp\left(-\left(\alpha_{\text{Abs}}W_{\text{Abs}}+\int_{-W_{Gd}}^{0}\alpha_{Gd}(x)dx\right)\right)\int_{0}^{W}\text{PA}(x)\alpha_{EA}(x)\exp\left(-\int_{0}^{x}\alpha_{EA}(x')dx'\right)dx\Bigg\}\end{aligned} \tag{6.1}$$

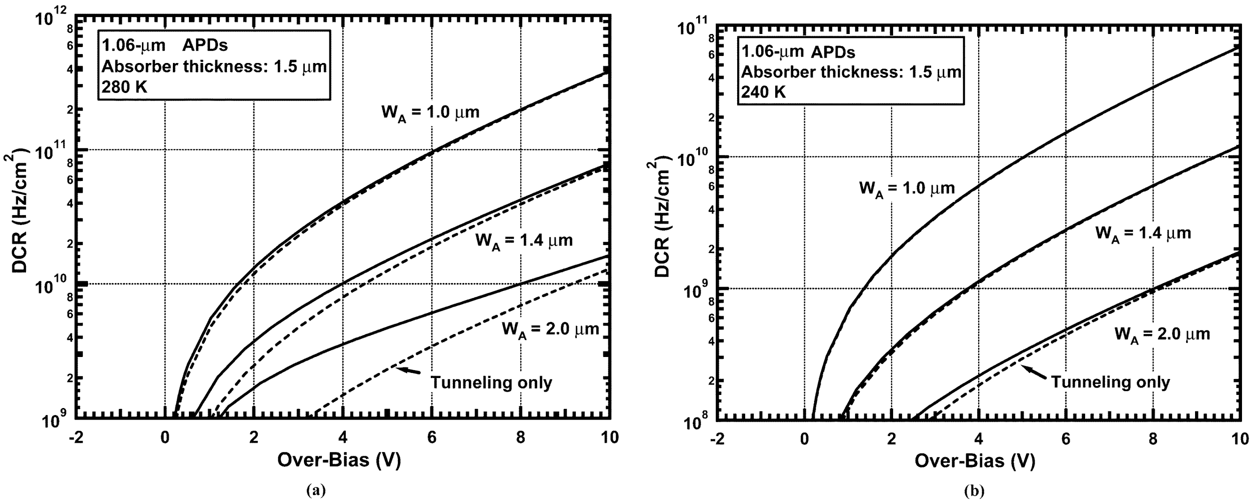

Fig. 11. Calculated DCRs versus overbias for 1.06-μm wavelength APDs with several different avalanche thicknesses and 1.5-μm-thick InGaAsP absorbers at (a) 280 K and (b) 240 K. Conservative values of N_T and τ were used in the calculations.

increases in PA with decreasing temperature. With a good AR coating the surface reflectivity R is less than 0.5%. The electroabsorption coefficient $\alpha_{EA}(x)$ in the InP high-field region was calculated based on the field at each point. At room temperature, electroabsorption coefficients are in the 10^3-cm^{-1} range for 1.06-μm light. As the temperature is reduced, electroabsorption in our devices decreases somewhat due to both the reduction in field (lower breakdown voltage) and a slight increase in bandgap energy.

For back-illuminated devices, PDE is given by (6.2), shown at the bottom of the page.

The absorption coefficients in our n$^+$ substrates α_{Sub} were measured to be around 7cm^{-1} at 1.064 μm. Loss in the nominally undoped n$^-$-substrates was negligible at 1.064 μm.

The PDE versus overbias calculations for a back-illuminated 1.06-μm device with an n$^+$-substrate, a 1.0-μm-thick avalanche region and a 1.5-μm-thick absorber region at temperatures of 273, 283, and 293 K are shown in Fig. 12, along with data taken on a back-illuminated device with an n$^+$-substrate. The data was taken with a focused spot. Scan measurements across the 20-μm -diameter diode as shown in Fig. 13 indicate a fairly flat PDE with a 2.0–2.5-μm inactive region around the periphery. Similar scans were obtained in both orthogonal directions. Active diameters that were 4–5-μm smaller than the actual physical diameters were consistently measured on diodes with different diameters and from different fabrication runs. DCRs scaled well with active area. Earlier data on front-illuminated devices showed PDEs around 50% in the 4–5-V overbias range. The lower PDE

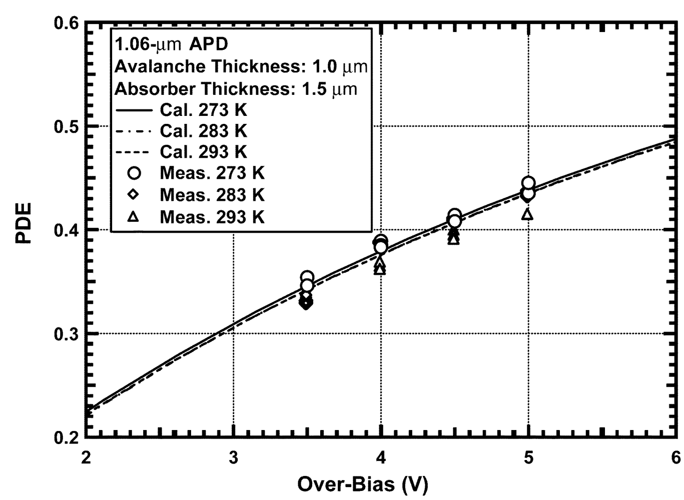

Fig. 12. Experimental and calculated photon detection efficiency PDE versus overbias at 273, 283, and 293 K for back-illuminated devices with an n$^+$-substrate.

on back-illuminated devices is due primarily to substrate absorption.

The PDE versus overbias calculated for front-illuminated and back-illuminated 1.06-μm devices with 1.0-, 1.4-, and 2.0-μm-thick avalanche regions at 295 K are shown in Fig. 14. All devices had a 1.5-μm-thick absorber region. The difference between the front-illuminated PDEs and back-illuminated

$$\begin{aligned}\mathrm{PDE} = &(1-R)\exp(-\alpha_{\mathrm{Sub}}W_{\mathrm{Sub}})\left\{\int_{-W}^{0}\mathrm{PA}(x)\alpha_{EA}(x)\exp\left(-\int_{-W}^{x}\alpha_{EA}(x')dx'\right)dx + \exp\left(-\int_{-W}^{0}\alpha_{EA}(x)\,dx\right)\right.\\ &\cdot\ \mathrm{PA}(0)\int_{0}^{W_{Gd}}\alpha_{Gd}(x)\exp\left(-\int_{0}^{x}\alpha_{Gd}(x')dx'\right)dx + \exp\left(-\left(\int_{-W}^{0}\alpha_{EA}(x)\,dx + \int_{0}^{W_{Gd}}\alpha_{Gd}(x)dx\right)\right)\\ &\left.\cdot\ \mathrm{PA}(0)(1-\exp(-\alpha_{\mathrm{Abs}}W_{\mathrm{Abs}}))\right\} \end{aligned} \tag{6.2}$$

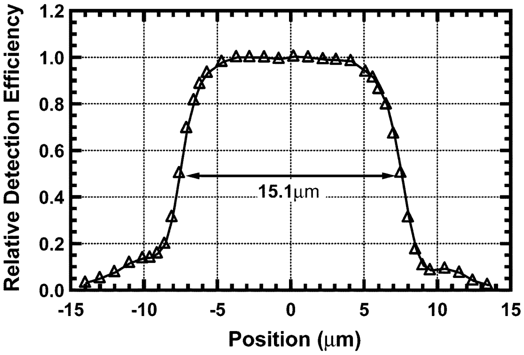

Fig. 13. PDE versus position obtained on a back-illuminated APD using a scanned focus spot.

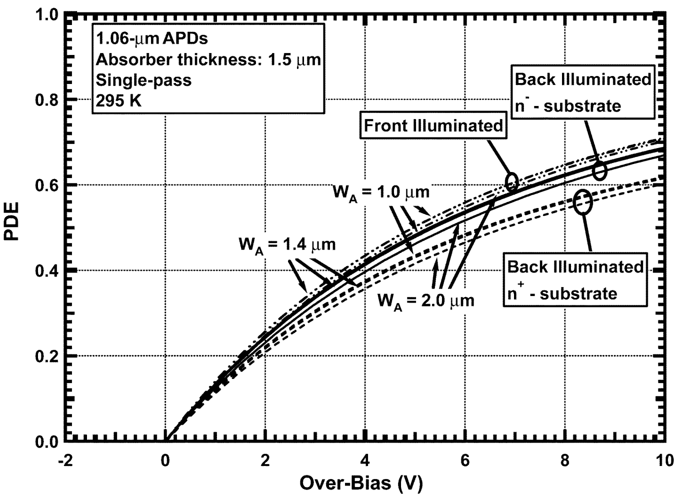

Fig. 14. Calculated photon detection efficiency PDE versus overbias at 295 K for front- and back-illuminated devices with avalanche thicknesses of 1.0-, 1.4-, and 2.0-μm-thick absorber layers. All devices had a 1.5-μm-thick absorber.

PDEs with an n$^-$-substrate is due to the light passing through the avalanche region first (more electroabsorption) in the back-illuminated device. The difference between the PDEs with an n$^-$-substrate and those with an n$^+$-substrate is due to differences in substrate loss. For front-illuminated devices, the PDE for devices with 1.0- and 1.4-μm-thick avalanche regions are almost identical. For back-illuminated devices, the devices with a 1.0-μm-thick avalanche region have slightly higher PDEs than those with a 1.4-μm avalanche region due to higher electroabsorption in the devices with thicker avalanche region. Devices with a thicker avalanche region have a lower PDE due to a reduced change of field with increased voltage which results in a lower PA in the thicker structures. As the temperature is reduced from 300 to 240 K, the PDEs in all cases increase by 2%–3% in the 3–6-V overbias range due to increases in PA. These PDE curves can be used with the DCR curves shown in Section V to assess the tradeoff between PDE and DCR for different avalanche thicknesses and desired maximum overbias. Note that from a DCR perspective it is desirable to use thicker avalanche regions if high overbiases are available from the ROIC being used. Although there is a drop off in PDE at a fixed overbias as the avalanche thickness increases, more substantial decreases in DCR means the device with the thicker avalanche region can be operated at higher

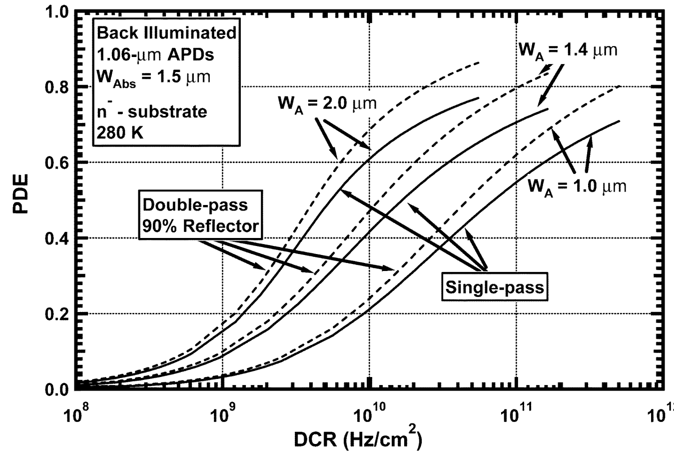

Fig. 15. Calculated PDE versus DCR at 280 K for 1.06-μm wavelength APDs with several different avalanche thicknesses and 1.5-μm-thick InGaAsP absorbers. PDE for both a single pass of the signal photons and a double pass, assuming a 90% reflection for the second pass, are shown.

overbiases more than making up the differences in PDE. With n$^-$-substrates and 1.4-μm-thick avalanche regions, PDEs and DCRs at 280 K of 53% and 2.2×10^{10} Hz/cm^2 (17 kHz for a 10-μm active area diameter), respectively, can be achieved with 5-V overbias. Corresponding values at 240 K are 56% and 1.3×10^{9} Hz/cm^2. With 2.0-μm-thick avalanche regions, PDEs $> 70\%$ can be achieved at 10-V overbias with corresponding DCRs similar to those obtained at 5-V overbias on devices with 1.4-μm-thick avalanche regions. PDE versus DCR at 280 K are shown in Fig. 15 for devices with 1.0-, 1.4-, and 2.0-μm-thick avalanche regions. The solid lines represent calculations for single-pass devices, while the dashed lines indicate PDE values for double-pass devices as described below.

So far we have dealt with devices that have 1.5-μm-thick absorber regions. This thickness was chosen to give a reasonable single-pass QE, while still permitting a near-optimal PDE. For a fixed overbias, more optimal designs are possible. To achieve higher QEs, one could increase the thickness of the absorber region, but this could result in higher DCR (near room temperature) and a decrease in PA(0). A simpler way to achieve higher QE would be a double-pass structure, in which the light passes though the absorber 2 times. Resonant structures that could reduce the volume of the absorber are also a consideration [36], [37], but since thermal generation in the absorber is not the major source of dark current in these 1.06-μm wavelength devices, resonant structures are not worth the added growth and fabrication complications. In our back-illuminated devices, a double-pass structure can be achieved by placing a high reflective metal contact (such as Ag or Au) on top of the diode mesa. Since there is a 2.5-μm inactive region around the periphery, the reflector metal does not have to cover the entire mesa. The n$^+$-InGaAs contact layer could be etched in the active region and reflector metal used as the contact as well. With a good reflector, QEs and, therefore, PDEs could be increased by $\approx 15\%$ with the same absorber thickness. Alternately, the absorber could be made thinner with only a small loss in QE, while increasing PA(0) (higher increase in avalanche field) and decreasing the DCR due to generation in the absorber at any fixed overbias. The calculated PDE versus overbias curves of

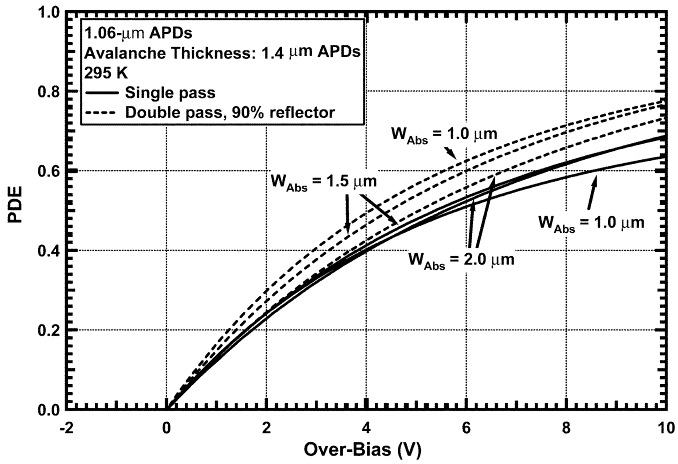

Fig. 16. Calculated PDE versus overbias at 295 K for 1.06-μm wavelength APDs with a 1.4-μm-thick avalanche region and several different thicknesses of the InGaAsP absorber. PDE for both a single pass of the signal photons and a double pass, assuming a 90% reflection for the second pass, are shown.

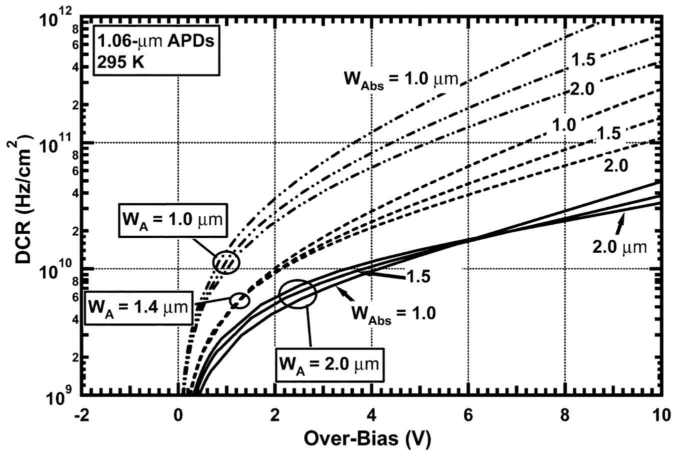

Fig. 17. Calculated DCRs versus overbias for 1.06-μm wavelength APDs with several different avalanche thicknesses and several different InGaAsP absorber thicknesses at 295 K.

a back-illuminated devices on an n$^-$-substrate with a 1.4-μm-thick avalanche region and 1.0-, 1.5-, and 2.0-μm absorber layers with and without a top reflector at 295 K are shown in Fig. 16. We actually looked at a number of absorber thicknesses ranging from 0.8 to 2.0 μm, but only three values are plotted for clarity. The reflectivity of the top reflector was assumed to be 90%. These double-pass devices have both higher QE and PDE compared to those of the single-pass devices. In single-pass devices, a near-optimum PDE is obtained over the entire bias range with an absorber thickness of 1.5 μm, while in double-pass devices a maximum PDE is achieved with a 1.0-μm-thick absorber region. DCR must also be considered, however, in choosing the absorber thickness just as it is in selecting the avalanche thickness. The DCRs at 295 K for devices with 1.0-, 1.4-, and 2.0-μm-thick avalanche regions and several different absorber thicknesses are show in Fig. 17. One might think that the DCR should decrease with reduced absorber thickness, but this is only true if generation in the absorber is a large contributor to the DCR. In these devices, tunneling in the avalanche region is dominant except in devices with the thickest avalanche regions, and the DCR decreases with increasing absorber thickness due to reductions in avalanche field at fixed overbias. Even with a 2.0-μm-thick avalanche region, tunneling plays a large role and there is no significant decrease in DCR with thinner absorbers. At lower temperatures, tunneling in the avalanche region will dominate even with thick avalanche regions.

VII. Conclusion

We have presented a model for the DCR and PDE of 1.06-μm InGaAsP–InP Geiger-mode avalanche photodiodes that gives a good fit to experimental data. The model can be used to evaluate the quality of the InP avalanche region and InGaAsP absorber region and to predict possible performance improvements with device modifications. Tunneling through defects in the avalanche region is an important contributor to DCR even at room temperature and dominates at lower temperatures. It can be fit to data with one adjustable parameter, N_T, the defect density. Generation in the absorber plays a role only around room temperature and can be fit with one adjustable parameter, τ, the effective lifetime. In 1.06-μm devices, electroabsorption in the avalanche region must be taken into account in calculating PDE. Substrate absorption must also be considered in back-illuminated devices. Back-illuminated devices, however, allow for a double pass through the absorber, which will increase the PDE. In general, Geiger-mode performance is better in devices with thicker avalanche regions. Even though devices with wider avalanche regions have a higher breakdown voltage and require a slightly higher overbias for the same PDE, a substantially lower DCR can be achieved for the same PDE. With current material, room temperature DCRs of less than 10 kHz with PDEs of $\approx$50% at 5-V overbias can be achieved in devices with 10-μm-diameter active areas. The DCR decreases with decreasing temperature while PDE increases slightly. Very low DCRs can be achieved at low temperatures. Reset time, however, increases with decreasing temperature [12] and this must be taken into consideration for applications that are sensitive to reset time. Higher PDEs can be achieved at higher overbias with modest increases in DCR in devices with thick avalanche regions. Lower DCRs are expected through continual improvements in material quality.

Acknowledgment

The authors wish to thank J. C. Aversa, K. Carbonari, J. E. Funk, J. Mahan, A. Napoleone, F. J. O'Donnell, and K. G. Ray for technical assistance.

References

[1] B. F. Aull, A. H. Loomis, D. J. Young, R. M. Heinrichs, B. J. Felton, P. J. Daniels, and D. J. Landers, "Geiger-mode avalanche photodiodes for three-dimensional imaging," *Lincoln Lab. J*, vol. 13, no. 2, pp. 335–350, 2002.

[2] M. A. Albota, B. A. Aull, D. G. Fouche, R. M. Heinrichs, D. G. Kocher, R. M. Marino, J. G. Mooney, N. R. Newbury, M. E. O'Brien, B. E. Player, B. C. Willard, and J. J. Zayhowski, "Three-dimensional imaging laser radars with Geiger-mode avalanche photodiode arrays," *Lincoln Lab. J.*, vol. 13, no. 2, pp. 351–367, 2002.

[3] K. A. McIntosh, J. P. Donnelly, D. C. Oakley, A. Napoleone, S. D. Calawa, L. J. Mahoney, K. M. Molvar, J. Mahan, R. J. Molnar, E. K. Duerr, G. W. Turner, M. J. Manfra, and B. F. Aull, "Arrays of III–V semiconductor Geiger-mode avalanche photodiodes," in *Proc. 16th Annu. Meeting of the IEEE Lasers and Electro-Optics Society*, 2003, vol. 2, pp. 686–687.

[4] J. P. Donnelly, K. A. McIntosh, D. C. Oakley, A. Napoleone, S. H. Groves, S. Vernon, L. J. Mahoney, K. Molvar, J. Mahan, J. C. Aversa, E. K. Duerr, Z. L. Liau, B. F. Aull, and D. C. Shaver, "1-μm Geiger-mode detector development," *Proc. SPIE*, vol. 5791, pp. 281–281, 2005.

[5] D. M. Boroson, R. S. Bondurant, and D. V. Murphy, G. S. Mecherle, C. Y. Young, and J. S. Stryjewski, Eds., "LDORA: A novel laser communications receiver array architecture," in *Proc. SPIE Free-Space Laser Communication Technologies XVI*, 2004, vol. 5338, pp. 16–28.

[6] S. Verghese, D. M. Cohen, E. A. Daular, J. P. Donnelly, E. K. Duerr, S. H. Groves, P. I. Hopman, K. E. Jensen, Z.-L. Liau, L. J. Mahoney, K. A. Mclntosh, D. C. Oakley, and G. M. Smith, "Geiger-Mode avalanche photodiodes for photon-counting communication," in *Proc. IEEE Lasers and Electro-Optics Society Summer Topical Meetings*, pp. 11–12, 2005, paper MA2.2.

[7] R. J. McIntyre, "Multiplication noise in uniform avalanche diodes," *IEEE Trans. Electron Devices*, vol. ED-13, no. 1, pp. 164–168, Jan. 1966.

[8] H. Dautet, P. Deschamps, B. Dion, A. D. MacGregor, D. MacSween, R. J. McIntyre, C. Trottier, and P. P. Webb, "Photon counting techniques with silicon avalanche photodiodes," *Appl. Opt.*, vol. 32, no. 21, pp. 3894–3900, Jul. 1993.

[9] S. Cova, A. Lacaita, and G. Ripamonti, "Trapping phenomena in avalanche photodiodes on nanosecond scale," *IEEE Electron Device Lett.*, vol. 12, pp. 685–687, Dec. 1991.

[10] S. Cova, M. Ghioni, A. Lacaita, C. Samori, and F. Zappa, "Avalanche photodiodes and quenching circuits for single-photon detection," *Appl. Opt.*, vol. 35, no. 12, pp. 1956–1976, Apr. 1996.

[11] Y. Kang, H. X. Lu, Y.-H. Lo, D. S. Bethune, and W. P. Risk, "Dark count probability and quantum efficiency of avalanche photodiodes for single-photon detection," *Appl. Phys. Lett.*, vol. 83, no. 14, pp. 2955–2957, Oct. 2002.

[12] K. E. Jensen, P. I. Hopman, E. K. Duerr, E. A. Dauler, J. P. Donnelly, S. H. Groves, L. J. Mahoney, K. A. McIntosh, K. M. Molvar, A. Napoleone, D. C. Oakley, S. Verghese, C. J. Vineis, and R. D. Younger, "Afterpulsing in Geiger-mode avalanche photodiodes for 1.06 μm wavelength," *Appl. Phys. Lett.*, vol. 88, pp. 133 503-1–133 503-3, Mar. 2006.

[13] K. A. McIntosh, J. P. Donnelly, D. C. Oakley, A. Napoleone, S. D. Calawa, L. J. Mahoney, K. M. Molvar, E. K. Duerr, S. H. Groves, and D. C. Shaver, "InGaAsP/InP avalanche photodiodes for photon counting at 1.06 μm," *Appl. Phys. Lett.*, vol. 81, no. 14, pp. 2505–2507, Sep. 2002.

[14] K. A. Mclntosh, J. P. Donnelly, D. C. Oakley, A. Napoleone, S. D. Calawa, L. J. Mahoney, K. M. Molvar, E. K. Duerr, and D. C. Shaver, "Development of Geiger-mode APD arrays for 1.06 μm," in *Proc. 15th Annu. Meeting of the IEEE Lasers and Electro-Optics Society*, 2002, vol. 2, pp. 760–761.

[15] I. Umebu, A. N. M. N. Choudhury, and P. N. Robson, "Ionization coefficients measured in abrupt InP junctions," *Appl. Phys. Lett.*, vol. 36, no. 4, pp. 302–303, Feb. 1980.

[16] C.-W. Kao and C. R. Crowell, "Impact ionization by electrons and holes in InP," *Solid-State Electron.*, vol. 23, no. 8, pp. 881–891, Aug. 1980.

[17] L. W. Cook, G. E. Burlman, and G. E. Stillman, "Electron and hole impact ionization coefficients in InP determined by photomultiplication measurements," *Appl. Phys. Lett.*, vol. 40, no. 7, pp. 589–591, Apr. 1982.

[18] C. A. Armiento and S. H. Groves, "Impact ionization in (100)-, (110)-, and (111)-oriented InP avalanche photodiodes," *Appl. Phys. Lett.*, vol. 43, no. 2, pp. 198–200, Jul. 1983.

[19] F. Osaka, T. Mikawa, and T. Kaneda, "Impact ionization coefficients of electrons and holes in (100)-Oriented $Ga_{1-x}In_xAs_yP_{1-y}$," *IEEE J. Quantum Eletron.*, vol. QE-21, pp. 1326–1338, Sep. 1985.

[20] F. Osaka and T. Mikawa, "Excess noise design of InP/GaInAsP/GaInAs avalanche photodiodes," *IEEE J. Quantum Electron.*, vol. QE-22, pp. 471–478, Mar. 1986.

[21] F. Zappa, P. Lovati, and A. Lacaita, "Temperature dependence of electron and hole ionization coefficients in InP," in *Conf. Proc. Int. Conf. Indium Phosphide and Related Materials*, Apr. 1996, pp. 628–631.

[22] Y. Takanashi and Y. Horikoshi, "Temperature dependence of ioization coefficients for InP and 1.3 mm InGaAsP avalanche photodiodes," *Jpn. J. Appl. Phys.*, vol. 20, pp. 1907–1913, Oct. 1981.

[23] Y. Okuto and C. R. Crowell, "Energy-conservation considerations in the characterization of impact ionization in semiconductors," *Phys. Rev.*, vol. B 6, no. 8, pp. 3076–3081, Oct. 1972.

[24] K. K. Thornber, "Applications of scaling to problems in high-field electronic transport," *J. Appl. Phys.*, vol. 52, no. 1, pp. 279–290, Jan. 1981.

[25] R. J. McIntyre, "A new look at impact ionization—Part I: A theory of gain, noise, breakdown probability, and frequency response," *IEEE Trans. Electron Devices*, vol. 45, no. 8, pp. 1623–1631, Aug. 1999.

[26] P. Yuan, K. A. Anselm, C. Hu, H. Nie, C. Lenox, A. L. Holmes, B. G. Streetman, J. C. Campbell, and R. J. McIntyre, "A new look at impact ionization-Part II: Gain and noise in short avalanche photodiodes," *IEEE Trans. Electron Devices*, vol. 46, no. 8, pp. 1632–1639, Aug. 1999.

[27] P. Yuan, C. C. Hansing, K. A. Anselm, C. V. Lenox, H. Nie, A. L. Holmes, B. G. Streetman, and J. C. Campbell, "Impact ionization characterisitics of III–V semiconductors for a wide range of multiplication region thicknesses," *IEEE J. Quantum Electron.*, vol. 36, no. 2, pp. 198–204, Feb. 2000.

[28] M. M. Hayat, B. A. E. Saleh, and M. C. Teich, "Effect of dead space on gain and noise of double-carrier-multiplication avalanche photodiodes," *IEEE Trans. Electron Devices*, vol. 39, no. 3, pp. 546–552, Mar. 1992.

[29] R. J. McIntyre, "On the avalanche initiation probability of avalanche diodes above the breakdown voltage," *IEEE Trans. Electron Devices*, vol. ED-20, no. 7, pp. 637–641, Jul. 1973.

[30] J. L. Moll, *Physics of Semiconductors*. New York: McGraw-Hill, 1964, pp. 240–253.

[31] S. M. Sze, *Physics of Semiconductor Devices*. New York: Wiley, 1981, pp. 520–527.

[32] N. Tabatabaie, G. E. Stillman, R. Chin, and P. D. Dapkus, "Tunneling in the reverse dark current of GaAlAsSb avalanche photodiodes," *Appl. Phys. Lett.*, vol. 40, no. 5, pp. 415–417, Mar. 1982.

[33] G. E. Stillman, C. M. Wolfe, C. O. Bozler, and J. A. Rossi, "Electroabsorption in GaAs and its application to waveguide detectors and modulators," *Appl. Phys. Lett.*, vol. 28, no. 9, pp. 544–546, May 1976.

[34] R. H. Kingston, "Electroabsorption in GaInAsP," *Appl. Phys. Lett.*, vol. 34, no. 11, pp. 744–746, Jun. 1979.

[35] G. E. Stillman and C. M. Wolfe, , R. K. Willardson and A. C. Beer, Eds., *Semiconductors and Semimetals*. New York: Academic, 1977, vol. 12, pp. 381–381.

[36] H. Nie, K. A. Anselm, C. V. Lenox, P. Yuan, C. Hu, G. Kinsey, B. G. Streetman, and J. C. Campbell, "Resonant-Cavity separate absorber, charge and multiplication avalanche photodiodes with high-speed and high gain-bandwidth product," *IEEE Photon. Technol. Lett.*, vol. 10, no. 3, pp. 409–411, Mar. 1998.

[37] K. A. Anselm, H. Nie, C. Lenox, C. Hansing, J. C. Campbell, and B. G. Streetman, "Resonant-cavity enhanced avalanche photodiodes grown by molecular beam epitaxy on InP for detection near 1.55 μm," *J. Vac. Sci. Technol. B.*, vol. 16, no. 3, pp. 1426–1429, May/Jun. 1998.

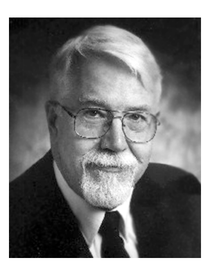

Joseph P. Donnelly (S'60–M'63–SM'88–F'90–LF'05) received the B.S. degree from Manhattan College, Bronx, NY, and the M.S. and Ph.D. degrees from Carnegie Mellon University, Pittsburgh, PA, all in electrical engineering.

He is currently a Senior Staff member at the Lincoln Laboratory, Massachusetts Institute of Technology, Lexington. Before joining the Lincoln Laboratory he was a NATO Postdoctoral Fellow at Imperial College, London, U.K. In addition to his position at Lincoln, he is an Adjunct Professor in the Physics Department, University of Massachusetts, Lowell. His current interests include high-power semiconductor lasers, integrated optics, and avalanche photodiodes.

Dr. Donnelly was a National Lecturer for the IEEE Electron Devices Society in 1979. In 2001, he was a Guest Associate Editor for a special issue of the IEEE JOURNAL OF SELECTED TOPICS IN QUANTUM ELECTRONICS on semiconductor lasers, and from 2002 to 2004 was an Associate Editor of the IEEE JOURNAL OF QUANTUM ELECTRONICS. He is a member of The Bohmesche Physical Society, Eta Kappa Nu, and Sigma Xi.

Erik K. Duerr received the B.S. degree from the University of Virginia, Charlottesville, and the S.M. and Ph.D. degrees from the Massachusetts Institute of Technology (MIT), Cambridge, in 1995, 1998, and 2002, respectively, all in electrical engineering. His graduate research concerned the development of sources and detectors for millimeter-wave and terahertz radiation.

He joined the MIT Lincoln Laboratory, Lexington, in 2003, and is currently developing avalanche photodiodes for single-photon detection using a variety of III–V material systems.

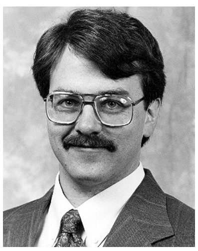

Alex McIntosh is a member of the Electro-Optical Materials and Devices Group at the Massachusetts Institute of Technology, Lincoln Laboratory, Lexington. His current research involves the development of arrays of Geiger-mode avalanche photodiodes. Since joining Lincoln Laboratory he has investigated high-speed infrared detectors, terahertz photomixers, and photonic crystal structures for infared and microwave applications.

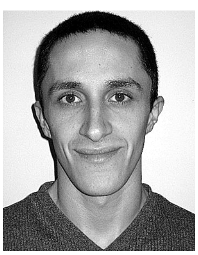

Eric A. Dauler received the S.B. and M.Eng. degrees in electrical engineering and computer science from the Massachusetts Institute of Technology (MIT), Cambridge. He is currently working toward the Ph.D. degree at MIT, working in the Quantum Nanostructures and Nanofabrication Group on superconducting nanowire single-photon detectors.

His research interests include single-photon detection, optical communication, and quantum optics. He has worked at the National Institute of Standards and Technology (1996–2000), the Boston University Photonics Center (1998–2001), and has been with the MIT Lincoln Laboratory since 2003.

Douglas C. Oakley received the B.A. degree in physics from the University of Maine, Orono, in 1991, and the M.S. degree in physics with a concentration in optics, specifically laser design and applications, from the University of Massachusetts, Lowell, in 1996. His thesis work entailed photoluminescence characterization of InP-based multiple quantum well structures, grown at the Massachusets Institute of Technology (MIT), Lincoln Laboratory, by MBE.

In the fall of 1996 he joined the MIT Lincoln Laboratory, Electro-Optical Materials and Devices Group, as an Assistant Research Staff working on growth of novel GaSb-based materials by OMVPE for the thermophotovoltaics research effort. In February of 2001, he was reassigned to run the InP-based OMCVD materials growth effort, producing novel InP/InGaAs/InGaAsP-based APD, PIN, laser, and modulator structures. He has recently received promotion to Associate Staff.

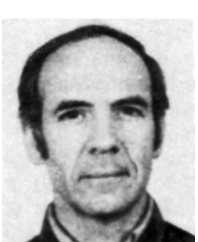

Steven H. Groves received the B.S. degree from Antioch College, Yellow Springs, OH, in 1957, and the A.M. and Ph.D. degrees from Harvard University, Cambridge, MA, in 1957, 1958, and 1963, respectively, all in physics.

From 1964 to 2006, he was with the Lincoln Laboratory, Massachusetts Institute of Technology, Lexington, aside from a visiting year at RSRE, Malvern, U.K., during 1970 to 1971. During this time, he studied transport phenomena, magnetooptical properties, and the band structure of zero and small bandgap semiconductors. In recent years, he worked on liquid-phase epitaxy and organometallic vapor phase epitaxy (OMVPE) crystal growth of III–V semiconductors, developing special growth techniques and impurity doping mechanisms. These InGaAsP/InP materials led to development of InP-based lasers, high-gain avalanche photodetectors, high-speed PIN detectors, and low-loss waveguide devices. He also worked on the characterization by X-ray and photoluminescence of heterojunctions and specially designed periodic structures on InGaAsP alloys. These techniques yielded information at the monomolecular thickness level, leading to the development of OMVPE InGaAsP/InP quantum well structures.

Dr. Groves was a member of the American Physical Society.

Christopher J. Vineis received the B.S.E. degree in materials science and engineering from the University of Pennsylvania, Philadelphia, and the Ph.D. degree in materials science and engineering from the Massachusetts Institute of Technology (MIT), Cambridge, in 1996 and 2001, respectively.

His areas of interest include materials growth and characterization and the relationship between device performance and materials properties, with a particular focus on electronic and optoelectronic materials and devices. He has experience with a variety of Si, III–V, and IV–VI materials systems, as well as lattice-mismatched epitaxy and metrology. He has been a Technical Staff Member at the MIT Lincoln Laboratory, Lexington, since 2005, and is currently focused on high-figure-of-merit nanostructured thermoelectric films for power generation and cooling applications, as well as Geiger-mode avalanche photodiodes for single-photon detection.

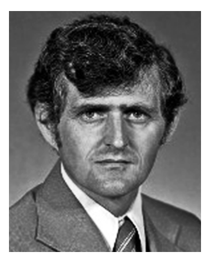

Leonard J. Mahoney received the B.S. degree (with honors) in mechanical engineering from Northeastern University, Boston, MA.

He joined the Lincoln Laboratory, Massachusets Institute of Technology, Lexington, in 1972, where he has worked on process development and fabrication of microwave and electro-optic devices. He is currently an Assistant Staff Member in the Electro-Optical Materials and Device Group, working on several InP- and GaN-based devices.

Karen M. Molvar received the B.S. degree in textile science from the University of Wisconsin, Madison, in 1978.

She joined the Lincoln Laboratory, Massachusets Institute of Technology, Lexington, in 1980, where she worked on a number of microwave devices and circuits including surface-oriented mixer diodes, frequency doublers, and FETs. She is currently a Project Technician in the Electro-Optical Materials and Device Group, working on GaN and InP devices.

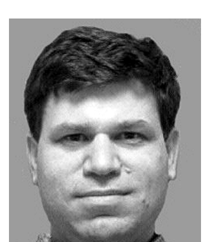

Pablo I. Hopman received the B.S. degree in physics from the University of California, Davis, and the Ph.D. degree in physics from Cornell University, Ithaca, NY. He is currently a Staff Member in the Advanced Concepts and Technology Group. He joined the Lincoln Laboratory, Massachusets institute of Technology, Lexington, in 2000. He most recently worked on the Mars Laser Communications Program where he served as Lead Engineer for the detector subsystem, and as a System Engineer for the ground receiver array. He has contributed to system studies, hardware development, and experimentation in several electro-optics areas, including photon-counting communications and space surveillance.

Katharine Estelle Jensen was born in New Haven, CT, in 1982. She received the A.B. degree in physics from Princeton University, Princeton, NJ, in 2004. In September 2006, she will begin Ph.D. work in physics at Harvard University, Cambridge, MA.

Since 2004, she has been a member of the Electro-optical Materials and Devices Group at the Lincoln Laboratory, Massachusetts Institute of Technology, Lexington

Ms. Jensen is a member of Sigma Xi.

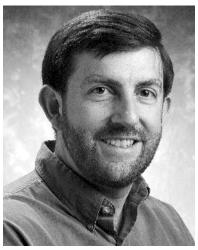

Gary M. Smith (S'93–M'95) received the B.S., M.S., and Ph.D. degrees in electrical engineering from the University of Illinois, Urbana-Champaign, in 1991, 1992, and 1996, respectively. His thesis work was performed on the design and fabrication of DFB and DBR stabilized semiconductor lasers.

After graduation he worked at Advanced Technology Materials, Inc., on optoelectronic devices in wide bandgap semiconductors. In 1999, he moved to Corning Lasertron to work on high-power 980-nm pump lasers. During his tenure at Lasertron he led the new product introduction of 250- and 500-mW fiber grating stabilized pump lasers. In 2004 he joined the Lincoln Laboratory, Massachusetts Institute of Technology, Lexington, to develop electro-optical semiconductor devices, and is primarily focusing on Geiger-mode avalanche photodiode arrays.

Dr. Smith is a member of the IEEE Lasers and Electro-Optics Society.

Simon Verghese (M'87) was born in Raleigh, NC, in 1965. He received the B.S. degree in physics and the B.S. degree and M.S. degrees in electrical engineering from North Carolina State University, Raleigh, in 1987, and in 1993 received the M.A. and Ph.D. degrees in physics from the University of California, Berkeley. His thesis work involved developing high-Tc superconducting bolometers for far-infrared spectroscopy, and measuring the response of superconducting tunnel junctions to picosecond voltage pulses.

In 1993, he was a Postdoctoral Associate in the Department of Electrical Engineering and Computer Science, Massachusetts Institute of Technology (MIT), Cambridge. In 1995, he joined the technical staff of MIT Lincoln Laboratory, Lexington, where his research interests include terahertz photomixers, resonant-tunneling diodes, infrared and UV avalanche photodiodes, and their associated read-out integrated circuits. After working for three years in fiber-optic communications at PhotonEx Corporation, he returned in 2003 to MIT Lincoln Laboratory where he is now Assistant Leader of the Electrooptical Materials and Devices Group.

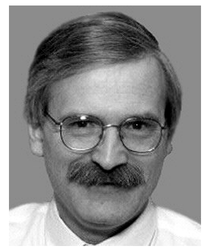

David C. Shaver (M'94–SM'04) received the S.B., S.M., and Ph.D. degrees in electrical engineering from the Massachusetts Institute of Technology, Cambridge. His areas of academic focus included microelectronics, circuit design, and neuroscience.

He began working at Lincoln Laboratory, Massachusetts Institute of Technology, Lexington, in 1977, in the area of submicrometer structure fabrication, where he applied X-ray and e-beam lithography to the fabrication of both electronic devices, such as submicrometer channel-length silicon MOSFETs and diffractive optics, including Fresnel zone-plates used for X-ray imaging. As an outgrowth of his work in electron-beam lithography, he developed electron-beam techniques for testing and repairing wafer-scale integrated circuits. In 1984, he joined a startup company, Micrion Corporation, where, as Chief Scientist and Director of Research, he was responsible for developing focused ion-beam and laser-beam microchemistry systems for photomask, microcircuit, and flat-panel display repair and modification. In 1988, he returned to the Lincoln Laboratory where he led a group which pioneered the development of 193-nm-wavelength optical lithography. In the fall of 1991, he became the Director of the Microelectronics Laboratory and Assistant Head of the Solid State Division. He was responsible for completing, equipping, and bringing online a new Class 10 microelectronics research facility and for overseeing all programs in silicon microelectronics and microfabrication technology. Since 1994, he has been the Head of the Solid State Division, and he oversees research in such varied areas as high-performance imaging sensors, deeply scaled silicon microelectronics, solid-state lasers, optoelectronics, photonics, superconductive devices, quantum computing, and biological agent sensors.